Aluminum Components in Bridgmanite Coexisting With Corundum and the CF-Phase With Temperature

Lin Wang[1,2] , **Zhaodong Liu[3]** , **Sanae Koizumi[4]** , **Tiziana Boffa Ballaran[1]** , **and Tomoo Katsura[1]**

[1]Bayerisches Geoinstitut, University of Bayreuth, Bayreuth, Germany, [2]Earth and Planetary Laboratory, Carnegie Institution Washington, Washington, DC, USA, [3]State Key Laboratory of Superhard Materials, Jilin University, Changchun, China, [4]Earthquake Research Institute, University of Tokyo, Tokyo, Japan

Abstract Phase relations in the $MgSiO_3$–$MgAl_2O_4$–Al_2O_3 system are investigated at 27 GPa and 2000–2600 K using a multi-anvil apparatus. The $AlAlO_3$ content in the bridgmanite increases from 8.6 to 20.0 mol% with increasing temperature from 2000 to 2600 K, while the $MgAlO_{2.5}$ content remains nearly constant, that is, 3–4 mol% at these temperatures. Therefore, the presence of an additional Al-bearing phase suppresses the oxygen vacancy substitution for Al^{3+} in bridgmanite. Conversely, significant amounts of the $Al_{8/3}O_4$ component can be dissolved into the calcium-ferrite type $MgAl_2O_4$–Mg_2SiO_4–$Al_{8/3}O_4$ phase (CF-phase), implying that the CF-phase likely contains some amount of vacancies. Therefore, the CF-phase could also be a candidate mineral for transporting volatiles into the lower mantle. Our results, combined with previous studies on Al-bearing bridgmanite, indicate that, once the Al per formula unit exceeds 0.12 in bridgmanite, the $MgAlO_{2.5}$ content remains nearly constant and the $AlAlO_3$ component becomes dominant.

Plain Language Summary Bridgmanite, the most abundant mineral in the Earth's mantle, can contain Al^{3+} in the forms of $MgAlO_{2.5}$ and $AlAlO_3$. To constrain the substitution mechanism of Al^{3+} in bridgmanite, we investigate the $MgAlO_{2.5}$ and $AlAlO_3$ contents in bridgmanite coexisting with a calcium-ferrite type phase and corundum at different temperatures. Our results demonstrate that the $MgAlO_{2.5}$ content reaches saturation (3–4 mol%) when an additional Al-bearing phase exists in the system.

1. Introduction

Bridgmanite is the most abundant mineral in the Earth's lower mantle. Consequently, it should govern the structure, dynamics, and evolution of the lower mantle. Accordingly, it is important to have the best possible knowledge concerning its chemistry. The major component of bridgmanite is $MgSiO_3$. However, it can incorporate Al^{3+}, Fe^{2+}, and Fe^{3+} as secondary elements. Hence, the chemistry of bridgmanite needs to be investigated in the Mg–Fe–Al–Si–O system. Because it too challenging to determine the effect of each individual element on the bridgmanite chemistry when investigating this five-component system, we need to start by investigating bridgmanite in simple systems and then expand to more complex systems. Another essential strategy in our series of investigations is to uniquely control the bridgmanite chemistry via the coexisting phases based on the phase rule. Using these strategies, the phase relations of the MgO–Al_2O_3–SiO_2, MgO–Fe_2O_3–SiO_2, and MgO–$FeAlO_3$–SiO_2 systems with specific coexisting phases as a function of pressure and temperature have been investigated in recent studies (Fei et al., 2020, 2021; Liu, Akaogi & Katsura, 2019; Liu, Ballaran, et al., 2019; Liu, Ishii, & Katsura, 2017; Liu et al., 2020).

Because of its simplicity, the MgO–Al_2O_3–SiO_2 system has been the most extensively investigated (Liu, Akaogi & Katsura, 2019; Liu, Ballaran, et al., 2019; Liu, Ishii, & Katsura, 2017; Liu, Nishi, et al., 2017). It has been found that bridgmanite accommodates Al as a charge-coupled (CC) component and/or an oxygen-vacancy (OV) component in the forms of $AlAlO_3$ and $MgAlO_{2.5}$, respectively (Hirsch & Shankland, 1991; Kojitani, Katsura, & Akaogi, 2007; Navrotsky et al., 2003; Panero et al., 2006; Yamamoto et al., 2003). The incorporation of Al into bridgmanite can affect its chemical and physical properties (Andrault et al., 2001, 2007; Ballaran et al., 2012; Daniel et al., 2004; Frost & Langenhorst, 2002; Frost et al., 2004; McCammon, 1997; Vanpeteghem et al., 2006; Xu et al., 1998). For example, the OV component considerably decreases the bulk modulus (Brodholt, 2000; Jackson et al., 2004; Walter et al., 2004, 2006; Yagi et al., 2004; Zhang & Weidner, 1999) and could help transport H_2O (Fu et al., 2019; Murakami et al., 2002; Navrotsky, 1999) and noble gases (Shcheka & Keppler, 2012) into

the lower mantle. Conversely, the geochemical and geophysical effects of the CC component appear insignificant. Therefore, it is essential to constrain the OV and CC contents in bridgmanite under various conditions.

The OV and CC contents are controlled by the MgO and Al_2O_3 activities of the system. With increasing Al_2O_3 activity, bridgmanite in the MgO–SiO_2–Al_2O_3 system coexists successively with only periclase, periclase and the CF-phase, the CF-phase and corundum, and ultimately only corundum. Coexisting either with periclase or corundum, maximizes the OV or CC components, respectively (Liu, Akaogi & Katsura, 2019; Liu, Ballaran, et al., 2019; Liu, Nishi, et al., 2017; Walter et al., 2006). When coexisting with periclase, the OV content increases from 3 to 6.5 mol% while the CC content decreases from 4 to 1.5 mol% with increasing temperature from 1700 to 2400 K at 27 GPa (Liu, Akaogi, & Katsura, 2019). Conversely, when coexisting with corundum, the CC content increases from 7.5 to 19 mol% under the same conditions, while the OV content remains close to zero (Liu, Nishi, et al., 2017). In an intermediate compositional system, where bridgmanite coexists with periclase and the CF-phase, only 1 and 2 mol% increases in the OV and CC contents, respectively, were observed under the same pressure–temperature ranges (Liu, Akaogi, & Katsura, 2019). Between coexistences with only corundum and with periclase and the CF-phase, there is a region in which bridgmanite coexists with the CF-phase and corundum; this region has not yet been studied. To obtain a comprehensive understanding of the bridgmanite chemistry, knowledge of the compositional variation of bridgmanite in this region as a function of pressure and temperature is useful. Furthermore, because the CF-phase is also a dominant phase in basaltic systems (Irifune & Ringwood, 1993), knowledge concerning the Al components of bridgmanite coexisting with the CF-phase is crucial to understand the chemical and geophysical properties of subducted slabs. In addition, this assemblage should also appear when crustal rocks with high Al_2O_3 content are subducted into the lower mantle.

In this study, we determine the OV and CC contents in bridgmanite coexisting with the CF-phase and corundum with increasing temperature from 2000 to 2600 K at a constant pressure of 27 GPa using a multi-anvil press. The results demonstrate that the OV content in bridgmanite remains essentially constant while the CC content increases with temperature. The combination of our results with those of previous studies (Grüninger et al., 2019; Liu, Akaogi, & Katsura, 2019) suggests that the OV content remains nearly constant when the Al per formula unit (pfu) in bridgmanite exceeds 0.12 regardless of temperature and that the CC component becomes dominant at high Al pfu.

2. Materials and Methods

Mixtures of MgO, Al_2O_3, and SiO_2 nanoparticles prepared at the Earthquake Research Institute, University of Tokyo, were used as starting materials. The preparation method is explained by Koizumi et al. (2010). The SiO_2:Al_2O_3:MgO weight ratios of the samples were 30:40:30 (sample group 1) and 20:55:25 (sample group 2). Namely, sample group 2 had a higher Al_2O_3 content than sample group 1. The grain size was approximately 50 nm to facilitate chemical equilibrium. These bulk compositions fall in the bridgmanite + CF-phase + corundum region based on Liu et al. (Liu, Akaogi & Katsura, 2019; Liu, Ballaran, et al., 2019).

High pressure–temperature experiments were conducted using a 15-MN multi-anvil press (IRIS-15) equipped with an Osugi-type guide-block system at the Bayerisches Geoinstitut (BGI), University of Bayreuth (Ishii et al., 2016, 2019). Sample groups 1 and 2 were loaded separately into two Pt capsules with outer and inner diameters of 1.0 and 0.8 mm, respectively. One end of the capsules was closed via arc welding. The capsules were placed in a vacuum furnace for 2 hr to remove adhesive water. The capsules were then placed on a hot plate at 100°C, and their open ends were closed and sealed via arc welding. Next, they were loaded into a MgO sleeve within a $LaCrO_3$ heater in a 5 wt.% Cr_2O_3-doped MgO octahedron with an edge length of 7.0 mm. A type-D thermocouple was inserted through the heater, and its junction was sandwiched by the two Pt capsules to monitor the sample temperature. The sample assembly was compressed to 27 GPa at ambient temperature using eight tungsten carbide anvils with edge lengths of 26 mm and truncations of 3.0 mm (Ishii et al., 2016). After reaching the target pressure, the samples were heated to target temperatures of 2000, 2300, 2500, and 2600 K at a ramping rate of 100 K/min. The heating durations were 2–25 hr (Table 1). Next, the samples were quenched to room temperature by switching off the heating power and decompressing to ambient pressure over a period of more than 16 hr.

The run products were mounted in Epoxy resin. Their cross sections were prepared by polishing with sandpaper and diamond pastes. Phases in the recovered samples were identified using a micro-focused X-ray diffractometer (Bruker AXS D8 Discover) equipped with a two-dimensional solid-state detector and a microfocus source of

Table 1
Experimental Conditions and Compositions of the Phases in the Run Products

Starting composition	Phase	Al_2O_3	MgO	SiO_2	Total	Al	Mg	Si	O	Brg / CF / Crn component 1	component 2	component 3
1675 (2000 K, 26 hr)												
sample group 1	Bri (n = 19)	10.78(52)	36.91(35)	52.56(38)	100.24(57)	0.211(9)	0.915(7)	0.874(7)	2.979(0)	$MgAlO_{2.5}$ 4.1(9)	$MgSiO_3$ 87.4(8)	$AlAlO_3$ 8.5(6)
	CF (n = 3)	53.18(107)	35.43(84)	12.10(49)	100.71(150)	1.474(16)	1.241(28)	0.286(13)	4.021(0)	Mg_2SiO_4 28.3(13)	$MgAl_2O_4$ 66.9(29)	$Al_{8/3}O_4$ 4.8(17)
	Cor (n = 8)	82.70(72)	7.46(39)	10.81(57)	100.96(67)	0.816(9)	0.093(5)	0.091(4)	1.499(0)	Al_2O_3 81.6(7)	$MgSiO_3$ 17.9(7)	
Sample group 2	Bri (n = 7)	10.68(43)	36.36(13)	52.03(26)	99.07(61)	0.212(7)	0.912(4)	0.876(4)	2.982(0)	$MgAlO_{2.5}$ 3.7(4)	$MgSiO_3$ 87.6(5)	$AlAlO_3$ 8.8(3)
	CF (n = 6)	52.47(62)	35.01(47)	12.60(117)	100.08(109)	1.465(28)	1.236(12)	0.298(24)	4.031(0)	Mg_2SiO_4 29.6(25)	$MgAl_2O_4$ 63.5(59)	$Al_{8/3}O_4$ 6.9(34)
	Cor (n = 13)	81.54(226)	7.37(66)	10.58(95)	99.49(88)	0.817(17)	0.093(9)	0.090(9)	1.498(0)	Al_2O_3 81.4(18)	$MgSiO_3$ 17.9(17)	
1679 (2300 K, 7 hr)												
sample group 1	Bri (n = 6)	16.96(22)	34.34(16)	49.25(30)	100.55(38)	0.332(4)	0.850(3)	0.818(4)	2.984(0)	$MgAlO_{2.5}$ 3.2(7)	$MgSiO_3$ 81.8(5)	$AlAlO_3$ 15.0(2)
	CF (n = 12)	49.36(54)	36.27(50)	15.12(60)	100.76(86)	1.370(15)	1.274(16)	0.356(12)	4.041(0)	Mg_2SiO_4 35.2(12)	$MgAl_2O_4$ 55.6(35)	$Al_{8/3}O_4$ 9.2(24)
	Cor (n = 11)	73.38(66)	10.78(58)	15.63(78)	99.80(88)	0.732(11)	0.136(6)	0.132(6)	1.498(0)	Al_2O_3 72.9(12)	$MgSiO_3$ 26.3(11)	
Sample group 2	Bri (n = 14)	16.55(43)	33.94(21)	49.13(47)	99.62(57)	0.327(8)	0.849(5)	0.824(5)	2.988(0)	$MgAlO_{2.5}$ 2.5(6)	$MgSiO_3$ 82.4(6)	$AlAlO_3$ 15.1(4)
	CF (n = 19)	48.87(75)	36.27(40)	15.31(55)	100.45(85)	1.361(18)	1.277(11)	0.362(12)	4.042(0)	Mg_2SiO_4 35.8(12)	$MgAl_2O_4$ 54.8(25)	$Al_{8/3}O_4$ 9.41(15)
	Cor (n = 21)	71.87(29)	10.85(13)	16.32(12)	99.04(29)	0.723(2)	0.138(2)	0.139(1)	1.500(0)	Al_2O_3 72.4(3)	$MgSiO_3$ 27.9(2)	
1662 (2300 K, 10 hr)												
sample group 1	Bri (n = 24)	17.72(70)	34.03(32)	48.45(67)	100.21(49)	0.348(14)	0.845(7)	0.807(9)	2.981(0)	$MgAlO_{2.5}$ 3.8(9)	$MgSiO_3$ 80.7(10)	$AlAlO_3$ 15.5(7)
	CF (n = 8)	47.52(34)	36.35(27)	15.60(15)	99.47(56)	1.336(5)	1.292(8)	0.372(3)	4.040(0)	Mg_2SiO_4 36.8(3)	$MgAl_2O_4$ 54.3(10)	$Al_{8/3}O_4$ 8.9(9)
	Cor (n = 17)	71.05(47)	11.83(25)	17.33(36)	100.21(47)	0.705(5)	0.149(3)	0.146(3)	1.499(0)	Al_2O_3 70.4(5)	$MgSiO_3$ 29.1(5)	
Sample group 2	Bri (n = 14)	17.43(38)	33.77(34)	47.97(58)	99.17(69)	0.346(8)	0.847(7)	0.807(6)	2.980(0)	$MgAlO_{2.5}$ 4.0(10)	$MgSiO_3$ 80.7(7)	$AlAlO_3$ 15.3(6)
	CF (n = 20)	47.45(48)	36.53(29)	15.54(23)	99.52(78)	1.333(8)	1.297(5)	0.370(4)	4.036(0)	Mg_2SiO_4 36.7(4)	$MgAl_2O_4$ 55.2(9)	$Al_{8/3}O_4$ 8.1(6)
	Cor (n = 17)	70.18(82)	11.77(20)	17.08(28)	99.03(80)	0.705(5)	0.150(3)	0.146(2)	1.498(0)	Al_2O_3 70.2(5)	$MgSiO_3$ 20(5)	
1672 (2500 K, 4 hr)												
sample group 1	Bri (n = 14)	19.21(50)	33.12(37)	47.75(34)	100.08(75)	0.378(8)	0.824(5)	0.797(6)	2.986(0)	$MgAlO_{2.5}$ 2.7(6)	$MgSiO_3$ 79.7(6)	$AlAlO_3$ 17.6(4)
	CF (n = 10)	46.94(61)	36.69(39)	16.82(14)	100.45(90)	1.309(7)	1.294(6)	0.398(5)	4.052(0)	Mg_2SiO_4 39.3(5)	$MgAl_2O_4$ 49.2(13)	$Al_{8/3}O_4$ 11.6(9)
	Cor (n = 14)	67.94(56)	12.71(21)	18.90(13)	99.55(71)	0.679(2)	0.161(2)	0.160(1)	1.500(0)	Al_2O_3 67.9(3)	$MgSiO_3$ 32.0(4)	
1670 (2600 K, 2 hr)												
sample group 1	Bri (n = 18)	21.87(36)	31.94(26)	45.69(36)	99.50(54)	0.433(7)	0.800(6)	0.767(3)	2.984(0)	$MgAlO_{2.5}$ 3.2(5)	$MgSiO_3$ 76.7(4)	$AlAlO_3$ 20.0(5)
	CF (n = 12)	43.65(46)	37.61(32)	19.19(19)	100.45(89)	1.218(4)	1.328(3)	0.454(3)	4.063(0)	Mg_2SiO_4 44.7(3)	$MgAl_2O_4$ 41.2(9)	$Al_{8/3}O_4$ 14.0(67)
	Cor (n = 8)	62.48(32)	15.58(10)	22.75(19)	100.81(53)	0.616(2)	0.194(1)	0.190(1)	1.498(0)	Al_2O_3 61.3(1)	$MgSiO_3$ 37.9(2)	

Note. Oxide analyses are reported in wt.%. The total cation numbers of bridgmanite (Brg) and corundum (Crn) are normalized to 2 and 3, respectively. The anion numbers of the calcium-ferrite type structured $MgAl_2O_4$–Mg_2SiO_4–$AlAlO_3$ (CF)-phase are normalized to 4. The numbers in parentheses represent the standard deviations for the last digits.
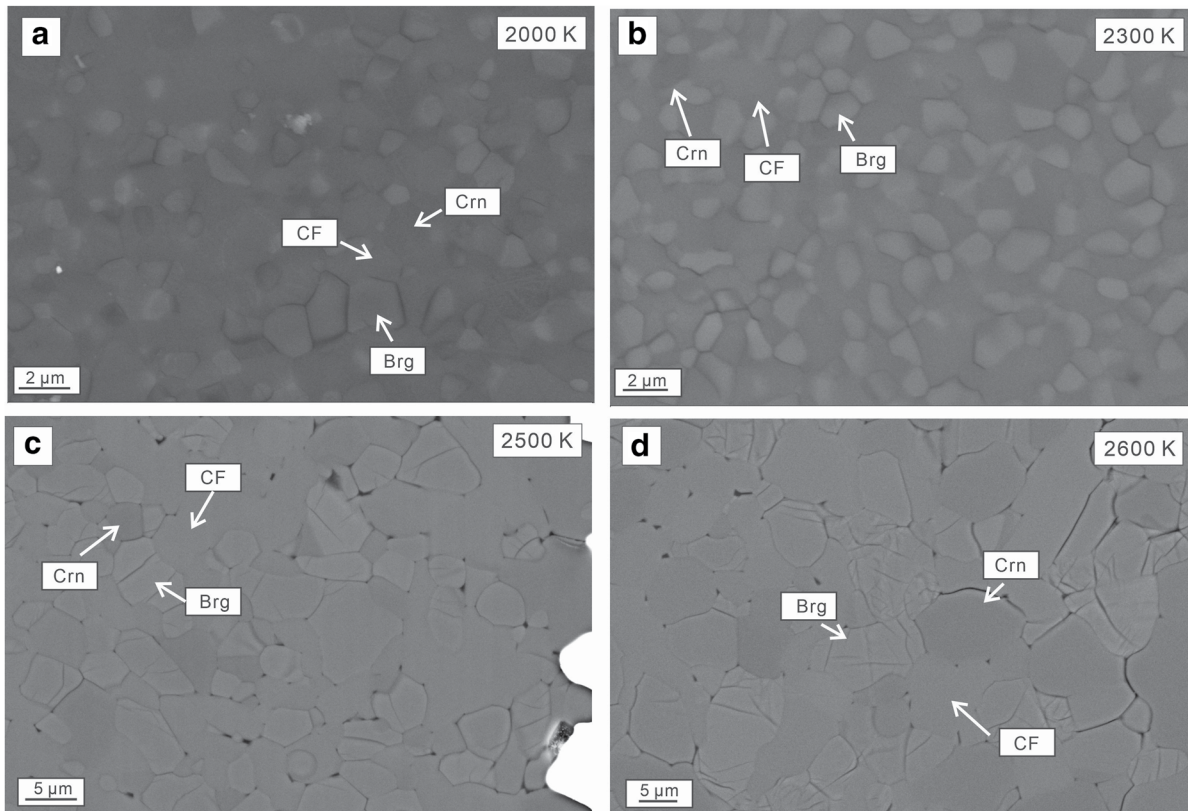
Figure 1. Back-scattered electron images of run products at various temperatures. Here, Brg indicates bridgmanite, Crn indicates corundum; and CF indicates calcium-ferrite type structured $MgAl_2O_4$–Mg_2SiO_4–$AlAlO_3$.

Co-Kα radiation operated at 40 kV and 500 μA at BGI. The exposure time was over 1 hr for each sample with a beam size of ~100 μm. The unit cell volumes of the CF-phase were determined by full-profile Le Bail fitting of the diffraction patterns using the GSAS software package on the EXPGUI interface (Larson & Von Dreele, 1994; Toby, 2001). Textures of the run products were observed using a LEO1530 scanning electron microscope with an energy-dispersive X-ray spectrometer (EDS) at BGI. Chemical compositions of the constituting minerals were measured using a JEOL 8530F field-emission electron probe microanalyzer (EPMA) at the Earth and Planets Laboratory, Carnegie Institute for Science, USA, with an acceleration voltage of 10 kV and a beam current of 15 nA with enstatite as the standard for Mg and Si and corundum as the standard for Al. Only regions close to the thermocouples were analyzed to eliminate the possible effect of the temperature gradient inside the cell assembly on the phase compositions.

3. Results

3.1. Phase Assemblages

Bridgmanite, corundum, and the CF-phase were identified in all run products from sample group 1 according to the X-ray diffraction patterns (Figure S1 in Supporting Information S2). These three phases were distinguished in back-scattered electron (BSE) images (Figure 1) combined with an EDS analysis. Bridgmanite appeared as the brightest grains. These grains showed a typical cleavage-like texture (Figures 1c and 1d) or very sharp grain-boundaries (Figures 1a and 1b), with sizes of 2–7 μm depending on the temperature. Corundum appeared as the darkest grains. The CF-phase exhibited an intermediate brightness and a smooth surface. The run products from sample group 2 showed granular mixtures of the three phases at 2000 and 2300 K, similar to those from sample group 1. However, the run products from sample group 2 at 2500 K showed stratification of the corundum, bridgmanite, and CF-phase (Figure S2A in Supporting Information S2). The run product from sample group 2 at 2600 K also showed a stratification that consisted of only corundum and the CF-phase (Figure S2B
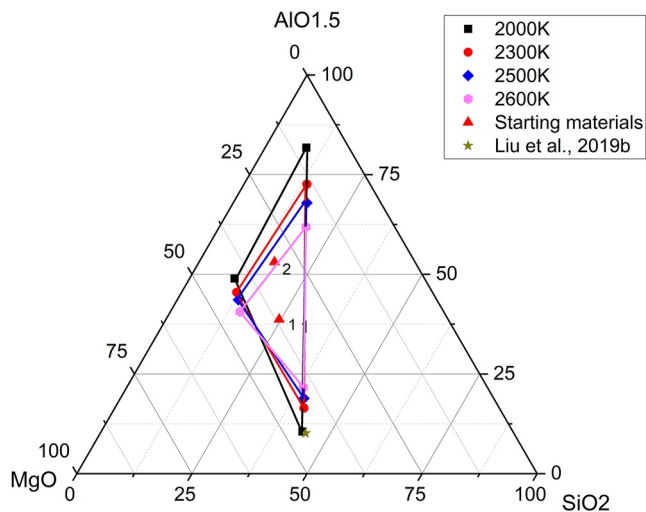
Figure 2. Ternary phase relations in the studied system at 27 GPa and different temperatures. Triangles 1 and 2 indicate the starting materials 1 and 2.

in Supporting Information S2). These corundum and CF-phase grains were abnormally large, ranging from 10 to 90 μm. These features imply that melting occurred in these samples. Sample group 2 should have the same solidus temperature as sample group 1 because the systems both have three phases with three components, that is, MgO, Al_2O_3, and SiO_2. Therefore, the melting of sample group 2 may have been caused by adhesive water; the removal of adhesive water before welding was likely insufficient in these samples.

3.2. Phase Compositions

Table 1 lists the compositions of bridgmanite and the coexisting phases in addition to the experimental conditions. Because of the possible melting at 2500 and 2600 K in sample group 2, we report only the phase compositions from sample group 1 at these temperatures. Figure 2 summarizes the phase compositions at different temperatures as a ternary phase diagram. The bulk composition of sample group 2 falls out of the ternary area at 2600 K, which agrees with the observation that only two phases are present in sample group 2.

The following pieces of evidence suggest chemical equilibrium among the phases. First, the phase compositions from different starting materials are essentially identical in the same runs. Second, the grains in the run products are more than 1.5 orders of magnitude larger than those of the starting materials (2–7 vs. 50 nm). Third, the BSE images indicate homogeneous composition within each grain. Fourth, the dihedral angles of ∼120° at the triple junction of the three phases indicate a textural equilibrium.

The Al pfu in bridgmanite increases from 0.211(9) to 0.433(7) with increasing temperature from 2000 to 2600 K (Figure 3a). The OV and CC contents were calculated according to the equations $Mg_xAl_zSi_yO_{x+1.5z+2y} = y$ $MgSiO_3 + (x − y) MgAlO_{2.5}$ (OV) $+ (z − x + y)/2 AlAlO_3$ (CC) and $x + y + z = 2$. Figure 3b shows the variation in the OV and CC contents with temperature. The OV contents are identical within the errors regardless of the temperature, that is, 3–4 mol% (Figure 3b). Conversely, the CC content increases from 8.6(5) to 20.0(5) mol% with increasing temperature from 2000 to 2600 K (Figure 3c). This demonstrates that the OV component has reached saturation and that the dissolved Al in the bridgmanite exists as the CC component.

Even though the CF-phase was treated as a solid solution in the $MgAl_2O_4$–Mg_2SiO_4 system (Kojitani, Hisatomi, & Akaogi, 2007), a $Al_{8/3}O_4$ component was observed in this study. The $Al_{8/3}O_4$, Mg_2SiO_4, and $MgAl_2O_4$ contents were calculated according to the equation $Mg_xAl_zSi_yO_{x+1.5z+2y} = y Mg_2SiO_4 + (x − 2y) MgAl_2O_4 + 3(z − 2x + 4y)/8$ $Al_{8/3}O_4$. The $Al_{8/3}O_4$ content increases from 6(3) to 14.0(6) mol% from 2000 to 2600 K (Figure 3c). As Figures 1c and 1d shows, the grain sizes of the CF-phase are larger than 5 μm, at least at temperatures of 2500 and 2600 K; therefore, the presence of this $Al_{8/3}O_4$ component is not due to possible errors in the EPMA analysis. The dissolved $Al_{8/3}O_4$ component in the CF-phase is also supported by the fact that the unit cell volume of the CF-phase decreases with increasing $Al_{8/3}O_4$ content (see Section 3.3). Kojitani, Hisatomi, and Akaogi (2007) showed that the unit cell volume of the CF-phase increases with its Mg_2SiO_4 content. The decrease in the unit cell volume of the CF-phase in this study should therefore be related to the increase in the $Al_{8/3}O_4$ content. Because the $Al_{8/3}O_4$ component has fewer cations than the other two CF-phase components, introducing the $Al_{8/3}O_4$ component into the CF-phase should produce cation vacancies, leading to smaller unit-cell volumes. The $MgAl_2O_4$ and Mg_2SiO_4 contents decreased from 65(5) to 41(1) mol% and increased from 29(2) to 44.7(3) mol%, respectively, with increasing temperature from 2000 to 2600 K (Figure 3d).

3.3. Unit-Cell Volumes

The unit cell volumes of bridgmanite have been extensively investigated (d'Amour et al., 1978; Irifune et al., 1996; Ito & Matsui, 1978; Ito et al., 1998; Kubo & Akaogi, 2000; Liu, Akaogi, & Katsura, 2019; Liu, Ballaran, et al., 2019; Liu, Nishi, et al., 2017; Walter et al., 2004; Weng et al., 1981; Yagi et al., 2004). Unit-cell-volume data from the literature and the current study (Table 2) can be fitted to the following linear function:

$$V^{Brg} [cm^3/mol] = 24.44 + x * X^{Brg}_{MgAlO_{2.5}} + y * X_{AlAlO_3}, \quad (1a)$$
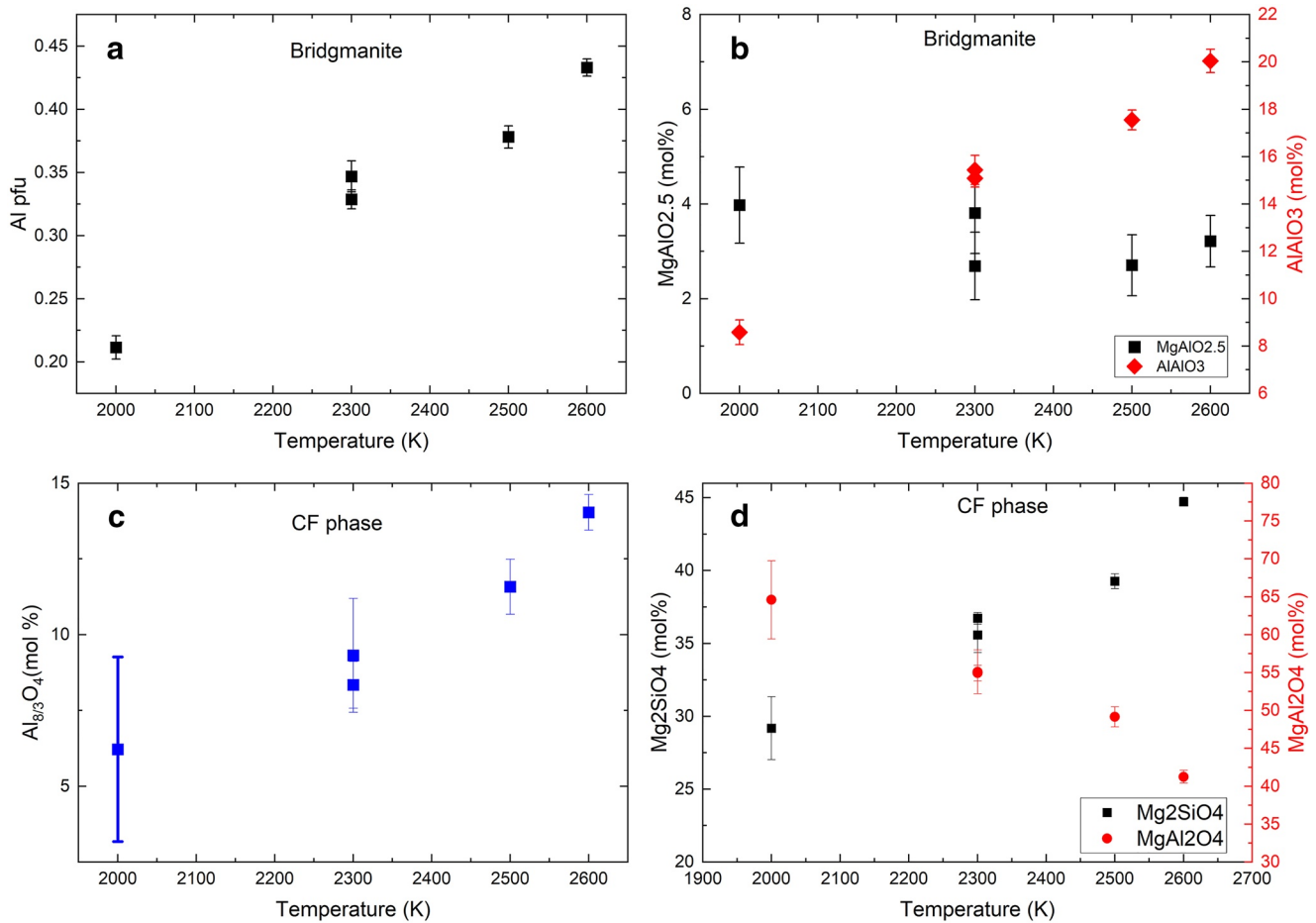
Figure 3. Compositional variation of bridgmanite and the CF-phase with increasing temperature: (a) Al per formula unit (pfu) in bridgmanite; (b) oxygen-vacancy and charge-coupled contents in bridgmanite; (c) $Al_{8/3}O_4$ content in the CF-phase; and (d) Mg_2SiO_4 and $MgAl_2O_4$ contents in the CF-phase.

where 24.44 cm³/mol is the molar volume of pure $MgSiO_3$ bridgmanite (Horiuchi et al., 1987), x and y are the excess molar volumes of the $MgAlO_{2.5}$ and $AlAlO_3$ endmembers relative to the $MgSiO_3$ endmember, respectively, and $X_{MgAlO_{2.5}}$ and X_{AlAlO_3} are the $MgAlO_{2.5}$ and $AlAlO_3$ contents, respectively, in mol%. The fitting yielded $x = 2.1(6)$ and $y = 0.9(2)$ and gives molar volumes of the $MgAlO_{2.5}$ and $AlAlO_3$ endmembers of $V_{MgAlO_{2.5}}^{Brg} = 26.5(6)$ cm³/mol and $V_{AlAlO_3}^{Brg} = 25.3(2)$ cm³/mol, respectively. As previously discussed in Liu, Akaogi, and Katsura (2019), the molar volumes of the $MgAlO_{2.5}$ and $AlAlO_3$ components are larger than that of the $MgSiO_3$ component, with that of the $MgAlO_{2.5}$ component being particularly large. These partial volumes agree with the decrease in the $MgSiO_{2.5}$ component with pressure (Liu, Ishii, & Katsura, 2017). The molar volumes of the $AlAlO_3$ and $MgSiO_3$ components of corundum are 25.64(1) and 25.96(8) cm³/mol, respectively (Liu, Nishi, et al., 2017). The volume reductions of the corundum–bridgmanite transition are 1.3% and 5.9% for

Table 2
Unit Cell Parameters of the CF-Phase and Bridgmanite Synthesized at Different Temperatures

	CF-phase				Bridgmanite			
T [K]	a [Å]	b [Å]	c [Å]	V [Å³]	a [Å]	b [Å]	c [Å]	V [Å³]
2000	9.995(2)	8.607(1)	2.788(0)	239.91(17)	4.771(3)	4.935(3)	6.926(3)	163.10(12)
2,300	10.005(1)	8.569(1)	2.787(0)	239.01(8)	4.764(2)	4.933(3)	6.943(3)	163.20(31)
2500	10.018(2)	8.569(1)	2.778(0)	238.53(25)	4.764(5)	4.929(7)	6.942(7)	163.04(23)

Note. Numbers in parentheses represent the standard deviation for the last digit(s).

the $AlAlO_3$ and $MgSiO_3$ components, respectively. Therefore, the volume decrease in the $MgSiO_3$ component is larger than that in the $AlAlO_3$ component. This is consistent with the fact that the formation of $AlAlO_3$ bridgmanite requires a much higher pressure than that of $MgSiO_3$ bridgmanite. The volume reduction of the corundum–bridgmanite transition in the $AlAlO_3$ component is also consistent with the fact that the pressure favors $AlAlO_3$ incorporation in bridgmanite (Liu, Nishi, et al., 2017).

The unit cell parameters of the CF-phase and bridgmanite synthesized at 2000, 2300, and 2500 K are summarized in Table 2. At these temperatures, the $Al_{8/3}O_4$ content in the CF-phase increases from 6(3) to 11.6(9) mol% and the Mg_2SiO_4 content increases from 29(2) to 39.3(5) mol%. The $MgAlO_{2.5}$ content in the bridgmanite decreases from 4.1(9) to 3.1 (5) mol%, and the $AlAlO_3$ content increases from 8.6(6) to 17.6(5) mol%.

To distinguish the effects of the Mg_2SiO_4 and $AlAlO_3$ components on the unit cell volume, we fitted the volumes of the CF-phase with a linear function:

$$V\left[cm^3/mol\right] = 36.13 + a * X_{Mg_2SiO_4} + b * X_{Al_{8/3}O_4}, \tag{1b}$$

where V is the molar volume of the CF-phase; 36.13 cm^3/mol is the molar volume of the pure $MgAl_2O_4$ CF-phase (Kojitani, Hisatomi, & Akaogi, 2007); a and b are the excess molar volumes of the Mg_2SiO_4 and $Al_{8/3}O_4$ endmembers, respectively, relative to the $MgAl_2O_4$ endmember; and $X_{Mg_2SiO_4}$ and X_{AlAlO_3} are the Mg_2SiO_4 and $Al_{8/3}O_4$ contents, respectively, in mol%. A fitting yields $a = 0.74(8)$ cm^3/mol and $b = -4.5(3)$ cm^3/mol. Namely, the molar volume of the CF-phase increases with the Mg_2SiO_4 content and significantly decreases with the $Al_{8/3}O_4$ content. By extrapolating Equation 1b to the Mg_2SiO_4 and $Al_{8/3}O_4$ endmembers, the molar volumes can be found: $V_{Mg_2SiO_4} = 36.87$ cm^3/mol and $V_{Al_{8/3}O_4} = 31.61$ cm^3/mol. Our estimated molar volume of Mg_2SiO_4 lies between those of Kojitani, Hisatomi, and Akaogi (2007) (36.49 cm^3/mol) and Yamada et al. (1983) (37.26 cm^3/mol). Note that the a-axis lattice parameter increases while the b- and c-axis lattice parameters decrease with the $Al_{8/3}O_4$ content. This indicates that the $Al_{8/3}O_4$ component has some preferred crystallographic sites. A further detailed study may better resolve the structure of this phase.

4. Discussion

4.1. Thermodynamics of Al-Bearing Bridgmanite

In this section, we formulate the thermodynamics of the OV and CC components in $MgSiO_3$ bridgmanite. The Gibbs free energy of the endmembers in bridgmanite and the interaction parameters can be obtained by fitting data from the present and previous studies (Liu, Akaogi & Katsura, 2019; Liu, Nishi, et al., 2017). The Al-bearing bridgmanite can be treated as a solid solution of the $MgSiO_3$, $AlAlO_3$, and $MgAlO_{2.5}$ components. Accordingly, the Gibbs free energy of these three endmembers as well as three macroscopic interaction parameters (Powell & Holland, 1993) are required to describe this system.

We first derive the interaction parameters between the $MgSiO_3$ and $AlAlO_3$ components ($W^{Brg}_{AlAlO_3-MgSiO_3}$) based on data from Liu, Nishi, et al. (2017). Then, we derive the interaction parameter between $AlAlO_3$ and $MgAlO_{2.5}$ ($W^{Brg}_{AlAlO_3-MgAlO_{2.5}}$) and between $MgSiO_3$ and $MgAlO_{2.5}$ ($W^{Brg}_{MgSiO_3-MgAlO_{2.5}}$) using data from the present study, where bridgmanite contains all three components. Finally, we derive the Gibbs free energy of the $MgAlO_{2.5}$ endmember ($G°^{Brg}_{MgAlO_{2.5}}$) using data from Liu, Akaogi, and Katsura (2019). The details of this deduction can be found in Supporting Information S1. The Gibbs free energies of the $MgSiO_3$ and $AlAlO_3$ endmembers are already known from the literature (Holland & Powell, 2011).

The interaction parameters of the $MgSiO_3$ and $AlAlO_3$ components can be derived using the data from Liu, Nishi, et al. (2017), where bridgmanite coexists only with corundum and both can be treated as binary solid solutions. At equilibrium,

$$\underset{Crn}{AlAlO_3} = \underset{Brg}{AlAlO_3}. \tag{2}$$
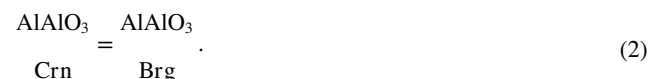
The Gibbs free energy of the reaction can be written as

$$\mu^{Crn}_{AlAlO_3} = \mu^{Brg}_{AlAlO_3}, \tag{3}$$

where μ_α^i [kJ/mol] is the chemical potential of the endmember α in phase i. The abbreviations Crn and Brg denote corundum and bridgmanite, respectively. Using the basics of thermodynamics and symmetric mixing modeling, the Gibbs free energy change of Equation 2 is expressed as

$$
\begin{aligned}
\Delta G_{R2} &= \mu_{AlAlO_3}^{Brg} - \mu_{AlAlO_3}^{Crn} \\
&= G_{AlAlO_3}^{\circ\,Brg} + RT\ln x_{AlAlO_3}^{Brg} + \left(1 - p_{AlAlO_3}^{Brg}\right)^2 W_{AlAlO_3-MgSiO_3}^{Brg} - G_{AlAlO_3}^{\circ\,Crn} \\
&\quad - RT\ln x_{AlAlO_3}^{Crn} - \left(1 - p_{AlAlO_3}^{Crn}\right)^2 W_{AlAlO_3-MgSiO_3}^{Crn},
\end{aligned}
\tag{4}
$$

where $G_\alpha^{\circ\,i}$ [kJ/mol] is the molar Gibbs free energy of the endmember α in phase i per mol at given pressure (P) and temperature (T) conditions. $G_{AlAlO_3}^{\circ\,Cor}$ and $G_{AlAlO_3}^{\circ\,Bri}$ can be found in the literature (Holland & Powell, 2011). x_α^i [no unit] is the mole fraction of the α component in phase i accounting for the mixing entropy, and γ_α^i [no unit] is the activity coefficient resulting from excess enthalpy deviating from ideal mixing. p_α^i [no unit] is the proportion of the α endmember in phase i (Powell & Holland, 1993).

By simultaneously minimizing ΔG_{R2} at different temperatures using data from Liu, Nishi, et al. (2017), a fitting yields $W_{AlAlO_3-MgSiO_3}^{Cor} = 49 \pm 16$ kJ/mol and $W_{AlAlO_3-MgSiO_3}^{Bri} = 26 \pm 3$ kJ/mol. The errors in the fitted interaction parameters arise from errors in the composition of each phase. Namely, we varied the compositions of each phase within their uncertainties and then calculated the corresponding interaction parameters. The reported interaction parameters and errors are the mean values and standard deviations of these calculated parameters. The higher $W_{AlAlO_3-MgSiO_3}^{Cor}$ value than $W_{AlAlO_3-MgSiO_3}^{Bri}$ value suggests that $x_{MgSiO_3}^{Crn}$ should be smaller than $x_{AlAlO_3}^{Brg}$, which is opposite to the observations (Table 1). This apparent discrepancy is caused by the smaller $G_{AlAlO_3}^{\circ\,Cor}$ than $G_{AlAlO_3}^{\circ\,Bri}$. However, the smaller volume of bridgmanite ($V_{AlAlO_3}^{Brg}$; 25.4 cm³/mol based on Holland and Powell (2011)) than corundum ($V_{AlAlO_3}^{Crn}$; 25.58 cm³/mol based on Holland and Powell (2011)) should increase $G_{AlAlO_3}^{\circ\,Cor}$ relative to $G_{AlAlO_3}^{\circ\,Bri}$. This increases and decreases $x_{AlAlO_3}^{Brg}$ and $x_{MgSiO_3}^{Crn}$, respectively, which agrees with the pressure dependence of AlAlO₃ in these two phases (Liu, Nishi, et al., 2017).

The interaction parameters $W_{AlAlO_3-MgAlO_{2.5}}^{Brg}$ and $W_{MgSiO_3-MgAlO_{2.5}}^{Brg}$ can be derived using the data in the present study where bridgmanite needs to be treated as a ternary system. The deduction follows the same method as above. Because the variation of $W_{MgSiO_3-MgAlO_{2.5}}^{Brg}$ does not significantly affect the fitting, we fixed it to 0 kJ/mol. $W_{AlAlO_3-MgAlO_{2.5}}^{Brg} = 104 \pm 12$ kJ/mol gives the best fitting. The errors in the fitted interaction parameters arise from the errors in the composition of each phase. The high $W_{AlAlO_3-MgAlO_{2.5}}^{Brg}$ value indicates that the Al_2O_3 component significantly suppresses $x_{MgAlO_{2.5}}^{Brg}$. This explains why $x_{MgAlO_{2.5}}^{Brg}$ is low in the Al_2O_3-rich system.

The Gibbs free energy of the bridgmanite MgAlO₂.₅ endmember ($G_{MgAlO_{2.5}}^{\circ\,Brg}$) can be derived from Liu, Akaogi, and Katsura (2019) combined with the above-derived interaction parameters. When bridgmanite coexists with periclase, the following reaction can be written:

$$
\underset{Brg}{MgAlO_{2.5}} = \underset{Per}{MgO} + \tfrac{1}{2}\underset{Brg}{AlAlO_3}.
\tag{5}
$$

Therefore, the standard-state Gibbs free energy change of Equation 5 is

$$
\Delta G_{R5}^{\circ} = \frac{1}{2} G_{AlAlO_3}^{\circ\,Brg} + G_{MgO}^{\circ\,Per} - G_{MgAlO_{2.5}}^{\circ\,Brg} = -RT\ln\left(\frac{a_{MgO}^{Per}\,a_{AlAlO_3}^{Brg}\,{}^{\frac{1}{2}}}{a_{MgAlO_{2.5}}^{Brg}}\right),
\tag{6}
$$

where a_i^j [no unit] is the activity of component i in phase j and is equal to $x_i^j \cdot \gamma_i^j$. Expanding the activity terms,

$$
G_{MgAlO_{2.5}}^{\circ\,Brg} = \frac{1}{2} G_{AlAlO_3}^{\circ\,Brg} + G_{MgO}^{\circ\,Per} + RT\ln x_{MgO}^{Per} + \frac{1}{2}\left(RT\ln x_{AlAlO_3}^{Brg} + RT\ln \gamma_{AlAlO_3}^{Brg}\right) - RT\ln x_{MgAlO_{2.5}}^{Brg} - RT\ln \gamma_{MgAlO_{2.5}}^{Brg}. \tag{7}
$$

$RT\ln\gamma_{MgO}^{Per}$ is omitted because the periclase is almost purely composed of MgO. $G_{AlAlO_3}^{\circ\,Bri}$ and $G_{MgO}^{\circ\,Per}$ can be found in Holland and Powell (2011). Using the composition data from Liu, Akaogi, and Katsura (2019), where bridgmanite coexists with the CF-phase and periclase, and the mixing model of bridgmanite from Huang et al. (2021), the
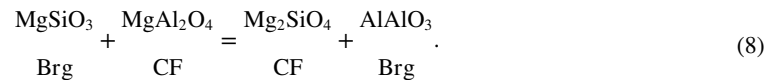
$G^{\circ\,\mathrm{Brg}}_{\mathrm{MgAlO}_{2.5}}$ values at 1700, 2000, and 2400 K are obtained as $-993.9(10)$, $-1058.7(5)$, and $-1154.2(12)$ kJ/mol, respectively. The errors arise from the analytical uncertainty in the phase compositions. By linearly fitting $G^{\circ\,\mathrm{Brg}}_{\mathrm{MgAlO}_{2.5}}$ with the temperature, one obtains $G^{\circ\,\mathrm{Brg}}_{\mathrm{MgAlO}_{2.5}} = -0.229(6)T - 602(13)$ kJ/mol.

To test the robustness of our thermodynamic modeling, we simulated the OV- and CC-content changes in bridgmanite with temperature at a fixed Al pfu (Figure S5A in Supporting Information S2) and their changes with Al pfu at a fixed temperature of 2000 K when bridgmanite coexists with only periclase at 27 GPa (Figure S5B in Supporting Information S2). The fitted curves generally agree with the experimental data at a temperature of 1700 K but deviate slightly at a higher temperature of 2400 K (Figure S5B in Supporting Information S2). This could be due to our assumption that periclase is composed of pure MgO. A certain amount of Al can be accommodated into periclase at high temperatures (Liu, Akaogi, & Katsura, 2019). Equation 5 could go to the left with increasing Al component in periclase because $\ln\gamma^{\mathrm{Per}}_{\mathrm{MgO}}$ becomes smaller, resulting a smaller $G^{\circ\,\mathrm{Brg}}_{\mathrm{MgAlO}_{2.5}}$ than the one we actually obtained. More data at higher temperatures are necessary to better constrain the thermodynamic parameters.

4.2. Compositional Changes of the CF-Phase With Temperature

The increase in the $\mathrm{Al}_{8/3}\mathrm{O}_4$ and $\mathrm{Mg}_2\mathrm{SiO}_4$ components in the CF-phase with temperature (Figures 3c and 3d) can be thermodynamically explained using our data by evaluating the entropy changes of the corresponding equations.

For the $\mathrm{Mg}_2\mathrm{SiO}_4$ component, the following reaction can be considered:

$$\underset{\mathrm{Brg}}{\mathrm{MgSiO}_3} + \underset{\mathrm{CF}}{\mathrm{MgAl}_2\mathrm{O}_4} = \underset{\mathrm{CF}}{\mathrm{Mg}_2\mathrm{SiO}_4} + \underset{\mathrm{Brg}}{\mathrm{AlAlO}_3}. \tag{8}$$

The standard-state Gibbs free energy change of Equation 8 can then be expressed as

$$\Delta G^{\circ}_{R8} = \mathrm{RT}\ln\frac{a^{\mathrm{Brg}}_{\mathrm{MgSiO}_3}\,a^{\mathrm{CF}}_{\mathrm{MgAl}_2\mathrm{O}_4}}{a^{\mathrm{CF}}_{\mathrm{Mg}_2\mathrm{SiO}_4}\,a^{\mathrm{Brg}}_{\mathrm{Al}_2\mathrm{O}_3}}$$

$$= \mathrm{RT}\ln\frac{x^{\mathrm{Brg}}_{\mathrm{MgSiO}_3}\,x^{\mathrm{CF}}_{\mathrm{MgAl}_2\mathrm{O}_4}}{x^{\mathrm{CF}}_{\mathrm{Mg}_2\mathrm{SiO}_4}\,x^{\mathrm{Brg}}_{\mathrm{Al}_2\mathrm{O}_3}} - \mathrm{RT}\ln\gamma^{\mathrm{CF}}_{\mathrm{Mg}_2\mathrm{SiO}_4} - \mathrm{RT}\ln\gamma^{\mathrm{Brg}}_{\mathrm{Al}_2\mathrm{O}_3} + \mathrm{RT}\ln\gamma^{\mathrm{Brg}}_{\mathrm{MgSiO}_3} + \mathrm{RT}\ln\gamma^{\mathrm{CF}}_{\mathrm{MgAl}_2\mathrm{O}_4}, \tag{9a}$$

where

$$\Delta G^{\circ}_{R8} = G^{\circ\,\mathrm{CF}}_{\mathrm{Mg}_2\mathrm{SiO}_4} + G^{\circ\,\mathrm{Brg}}_{\mathrm{AlAlO}_3} - G^{\circ\,\mathrm{CF}}_{\mathrm{MgAl}_2\mathrm{O}_4} - G^{\circ\,\mathrm{Brg}}_{\mathrm{MgSiO}_3}. \tag{9b}$$

Because of the coupled substitution, we assume the molecular mixing model (Powell, 1978) for the CF-phase. For bridgmanite,

$$x^{\mathrm{Brg}}_{\mathrm{MgSiO}_3} = x_{\mathrm{Mg,A}}\,x_{\mathrm{Si,B}}. \tag{10}$$

Here, $x^{\mathrm{Brg}}_{\mathrm{Si,B}}$ is the mole fraction of Si on the B site. The expression of the $\mathrm{RT}\ln\gamma$ terms have the form of Equation (S10) in Supporting Information S1. The interaction parameters of bridgmanite are derived in Section 4.1.

According to Davies and Navrotsky (1983), the interaction parameter of the CF-phase, $W^{\mathrm{CF}}_{\mathrm{A-B}}$, is assumed to be

$$W^{\mathrm{CF}}_{\mathrm{A-B}} = 100.8\Delta V - 0.4\,\mathrm{kJ/mol}, \tag{11}$$

where

$$\Delta V = \frac{V_{\mathrm{A}} - V_{\mathrm{B}}}{(V_{\mathrm{A}} + V_{\mathrm{B}})/2}. \tag{12}$$

Here, V_{A} and V_{B} are the molar volumes of the larger and smaller components, respectively. We then find that $W^{\mathrm{CF}}_{\mathrm{Mg}_2\mathrm{SiO}_4-\mathrm{Al}_{8/3}\mathrm{O}_4}$, $W^{\mathrm{CF}}_{\mathrm{Mg}_2\mathrm{SiO}_4-\mathrm{MgAl}_2\mathrm{O}_4}$, and $W^{\mathrm{CF}}_{\mathrm{Al}_{8/3}\mathrm{O}_4-\mathrm{MgAl}_2\mathrm{O}_4}$ are 3.5, 0.1, and 3.0 kJ/mol, respectively. As a result, ΔG°_{R8}
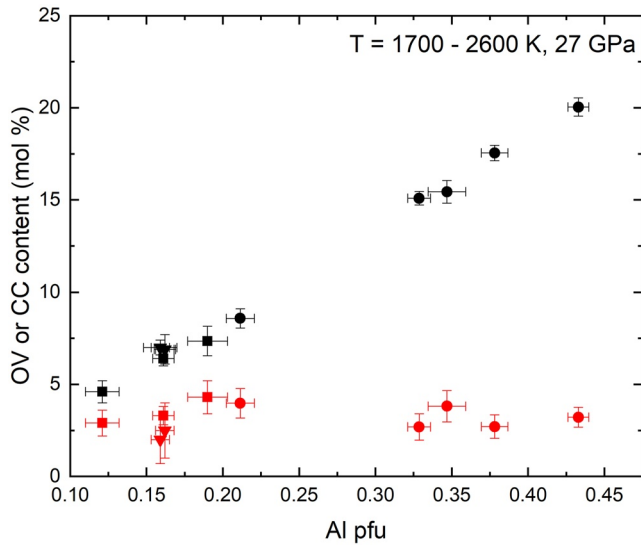
Figure 4. Contents of oxygen-vacancy (red) and charge-coupled (black) in bridgmanite coexisting with an additional Al-bearing phase with different Al pfu values in bridgmanite. The squares, triangles, and circles indicate data from Liu, Akaogi, and Katsura (2019), where bridgmanite coexists with the CF-phase and periclase, from Liu, Ballaran, et al. (2019), where bridgmanite coexists with the CF-phase and periclase, and from our study, respectively.

can be calculated using Equation 9a and is found to decrease from 26(2) to 8(1) kJ/mol from 2000 to 2600 K (Figure S6 in Supporting Information S2 and Table S1). The errors in ΔG°_{R8} arise from the analytical uncertainty in the phase compositions. Accordingly, $\Delta S^\circ_{R8} = -\left(\frac{\partial \Delta G^\circ_{R8}}{\partial T}\right)_P = 27 \pm 5\,\text{J/mol/K}$, where the error arises from the linear fitting itself. The positive entropy change of Equation 8 explains the increase in the Mg_2SiO_4 content in the CF-phase with temperature (Figure S6 in Supporting Information S2).

The increase in the $AlAlO_3$ content in the CF-phase can be explained by the reaction

$$\underset{\text{Crn}}{AlAlO_3} = \frac{3}{4}\underset{\text{CF}}{Al_{8/3}O_4}. \tag{13}$$
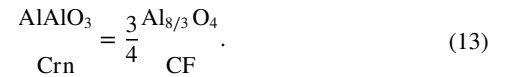
The standard-state Gibbs free energy change of Equation 13 can then be expressed as

$$
\begin{aligned}
\Delta G^\circ_{R13} &= RT\ln\frac{a^{\text{Crn}}_{AlAlO_3}}{(a^{\text{CF}}_{Al_{\frac{8}{3}}O_4})^{\frac{3}{4}}} \\
&= RT\ln\frac{x^{\text{Crn}}_{AlAlO_3}}{(x^{\text{CF}}_{Al_{8/3}O_4})^{3/4}} - \frac{3}{4}RT\ln\gamma^{\text{CF}}_{Al_{8/3}O_4} + RT\ln\gamma^{\text{Crn}}_{AlAlO_3},
\end{aligned}
\tag{14a}
$$

where

$$\Delta G^\circ_{R13} = \frac{3}{4}G^{\circ\,\text{CF}}_{Al_{8/3}O_4} - G^{\circ\,\text{Crn}}_{AlAlO_3}. \tag{14b}$$

Assuming the molecular mixing model for the $Al_{8/3}O_4$ component in the CF-phase, ΔG°_{R13} decreases from 31(7) kJ/mol to 27(1) kJ/mol from 2000 to 2600 K (Figure S6 in Supporting Information S2 and Table S1). Accordingly, $\Delta S^\circ_{R13} = -\left(\frac{\partial \Delta G^\circ_{R21}}{\partial T}\right)_P = 6 \pm 2\,\text{J/mol/K}$, indicating that higher temperatures favor the $Al_{8/3}O_4$ component in the CF-phase.

4.3. Aluminum Substitution Mechanism in Bridgmanite

Our observation that the increase in the Al pfu in bridgmanite only affects its $AlAlO_3$ content (Figure 4) indicates that the $MgAlO_{2.5}$ component has reached actual "saturation" when the Al pfu in bridgmanite reaches a particular value. The Al pfu in bridgmanite is determined by the activity of Al_2O_3 in the system ($a^{\text{system}}_{Al_2O_3}$), namely, the coexisting phases. When $a^{\text{system}}_{Al_2O_3}$ is low, bridgmanite coexists with periclase and is the only reservoir of Al_2O_3. Under such circumstances (Al pfu < 0.12), referred to as stage I here, the $AlAlO_3$ and $MgAlO_{2.5}$ contents increase with increasing Al pfu (Liu, Akaogi, & Katsura, 2019). Further increases in $a^{\text{system}}_{Al_2O_3}$ produce another Al_2O_3-host phase, that is, the CF-phase (Liu, Akaogi & Katsura, 2019; Liu, Ballaran, et al., 2019). Under such circumstances, referred to as stage II, the increase in the Al pfu in bridgmanite only slightly increases the $MgAlO_{2.5}$ content but significantly increases the bridgmanite $AlAlO_3$ content. With further increases in $a^{\text{system}}_{Al_2O_3}$, referred to as stage III, the coexisting Al_2O_3 phase changes to corundum and the CF-phase while the $MgAlO_{2.5}$ content remains nearly constant. Note that the $MgAlO_{2.5}$ contents in bridgmanite are essentially identical within the error in stages II and III (Figure 4). We conclude that the $MgAlO_{2.5}$ content reaches the solubility limit of 3–4 mol% once the Al pfu is higher than 0.12, where bridgmanite coexists with the Al-bearing phases (Figure 4).

The nearly constant $MgAlO_{2.5}$ content in bridgmanite coexisting with the CF-phase can be explained by Equation 8. Equation 8 suggests that the reacted amount of the $MgSiO_3$ component is equal to the produced $AlAlO_3$ component in the bridgmanite. If the produced $AlAlO_3$ is solely accommodated by bridgmanite, its $MgAlO_{2.5}$ content should remain constant. When bridgmanite does not coexist with corundum but coexists with only the

CF-phase, a small amount of AlAlO$_3$ can be dissolved by the CF-phase, leading to a small increase in MgAlO$_{2.5}$ in the bridgmanite (Liu, Ballaran, et al., 2019). When bridgmanite coexists with corundum, the AlAlO$_3$ in the CF-phase can be supplied by corundum (Equation 13). Therefore, the MgAlO$_{2.5}$ content in the bridgmanite remains unchanged (Figure 4).

Our results demonstrate that the CC content is always larger than the OV content in bridgmanite when it coexists with an Al-bearing phase, regardless of the temperature. This indicates that the CC component is the dominant Al-bearing component in bridgmanite in slabs. Because the CC substitution mechanism has only a mild effect on the bridgmanite elasticity (Walter et al., 2004, 2006), Al substitution in bridgmanite should affect only slightly the elastic properties of bridgmanite and, accordingly, the seismic wave velocity in slabs.

5. Implications

5.1. Noble Gas Storage Ability of Bridgmanite and the CF-Phase in Subducting Slabs

Even though the system investigated in this study is Al$_2$O$_3$ rich and cannot be directly compared to mid-ocean ridge basalt (MORB; Sun et al., 1979) or pyrolite (Sun, 1982), some local regions in subducting slabs could have the phase assemblage found in the present system. Some eclogites (Janák et al., 2012) contain the garnet + corundum + spinel phase assemblage, which should transform to bridgmanite + corundum + CF-phase under lower-mantle conditions. In such environments, bridgmanite should contain an OV component of up to 4 mol%. Because argon could be stored in bridgmanite oxygen vacancies (Shcheka & Keppler, 2012), the presence of the OV component could provide a possible mechanism for argon storage in bridgmanite. In fact, an OV component of 4 mol% can accommodate 0.8 wt.% argon, which is close to the experimentally observed solubility (Shcheka & Keppler, 2012).

The CF-phase could play a more critical role in transferring noble gases into the deep mantle than bridgmanite because the CF-phase can contain significant amounts of the Al$_{8/3}$O$_4$ component, introducing vacancies in the structure. If the sizes of the vacancies are comparable to the radii of noble gases, the Al$_{8/3}$O$_4$-bearing CF-phase could be an important reservoir of noble gas in the lower mantle. Further studies on the structure of such a CF-phase and its noble gas solubility are needed to test this hypothesis.

5.2. Implication of Oceanic Crust Separation From the Lithosphere in the Lower Mantle

The accumulation of basaltic crusts at the core–mantle boundary (CMB) has been proposed as an explanation for the large low-shear-wave provinces (Jones et al., 2020). Basaltic crusts are denser than the ambient mantle below 720 km (Ishii et al., 2022). If the basaltic layer separates from the underlying lithosphere in the slab, this density contrast would lead crustal materials to sink down to the CMB. Weak cubic CaSiO$_3$ is one possible separation mechanism. However, basaltic crusts contain not only davemaoite but also large portions of bridgmanite and the CF-phase. Our results could provide some hints concerning the strength of bridgmanite and the CF-phase from the viewpoint of crystal defects.

The mineral strength is controlled by the diffusion of the slowest species (e.g., Herring, 1950). Accordingly, increasing vacancy concentration is expected to decrease the mineral strength. Our results demonstrate that the OV content in bridgmanite coexisting with the CF-phase is approximately 3 mol% at the top of the lower mantle. Even though the bridgmanite in the surrounding upper lower mantle can contain up to 7 mol% OV content because it coexists with periclase (Liu, Akaogi & Katsura, 2019; Liu, Ballaran, et al., 2019), this difference decreases with depth (Liu, Ishii, & Katsura, 2017). Therefore, the strength of bridgmanite in the basaltic layer is more or less similar to that in the surrounding mantle at greater depth.

Conversely, the CF-phase could be very soft. The CF-phase becomes a major phase in the MORB layer after 26 GPa. Our results demonstrate that significant numbers of vacancies can exist in the CF-phase, implying that the CF-phase could be very soft. Combined with the soft cubic CaSiO$_3$, the strength of the MORB layer is expected to be much lower than that of the surrounding mantle, which primarily consists of bridgmanite and ferropericlase. This viscosity contrast makes it easy for the oceanic crust to be peeled off the underlying lithosphere by shear forces.

The above hypothesis is based on qualitative observations. To constrain the strength of oceanic crusts, deformation experiments on the CF-phase and MORB mineral aggregates are necessary. In addition, the incorporation of Na and K into the CF-phase, as well as into bridgmanite, could change the vacancy concentrations in the CF-phase and the bridgmanite. Further studies of more realistic systems are therefore needed to illustrate slab dynamics.

Data Availability Statement

All the data are listed in the manuscript and the online supporting information. The EPMA and XRD data set for this research are given in the Zenodo (https://doi.org/10.5281/zenodo.7512647).

References

Andrault, D., Bolfan-Casanova, N., Bouhifd, M. A., Guignot, N., & Kawamoto, T. (2007). The role of Al-defects on the equation of state of Al–(Mg, Fe)SiO$_3$ perovskite. *Earth and Planetary Science Letters*, *263*(3–4), 167–179. https://doi.org/10.1016/j.epsl.2007.08.012

Andrault, D., Bolfan-Casanova, N., & Guignot, N. (2001). Equation of state of lower mantle (Al, Fe)-MgSiO3 perovskite. *Earth and Planetary Science Letters*, *193*(3–4), 501–508. https://doi.org/10.1016/s0012-821x(01)00506-4

Ballaran, T. B., Kurnosov, A., Glazyrin, K., Frost, D. J., Merlini, M., Hanfland, M., & Caracas, R. (2012). Effect of chemistry on the compressibility of silicate perovskite in the lower mantle. *Earth and Planetary Science Letters*, *333*, 181–190. https://doi.org/10.1016/j.epsl.2012.03.029

Brodholt, J. P. (2000). Pressure-induced changes in the compression mechanism of aluminous perovskite in the Earth's mantle. *Nature*, *407*(6804), 620–622. https://doi.org/10.1038/35036565

d'Amour, H., Schiferl, D., Denner, W., Schulz, H., & Holzapfel, W. (1978). High-pressure single-crystal structure determinations for ruby up to 90 kbar using an automatic diffractometer. *Journal of Applied Physics*, *49*(8), 4411–4416. https://doi.org/10.1063/1.325494

Daniel, I., Bass, J. D., Fiquet, G., Cardon, H., Zhang, J., & Hanfland, M. (2004). Effect of aluminium on the compressibility of silicate perovskite. *Geophysical Research Letters*, *31*(15), L15608. https://doi.org/10.1029/2004gl020213

Davies, P., & Navrotsky, A. (1983). Quantitative correlations of deviations from ideality in binary and pseudobinary solid solutions. *Journal of Solid State Chemistry*, *46*(1), 1–22. https://doi.org/10.1016/0022-4596(83)90122-6

Fei, H., Liu, Z., Huang, R., Kamada, S., Hirao, N., Kawaguchi, S., et al. (2021). Pressure destabilizes oxygen vacancies in bridgmanite. *Journal of Geophysical Research: Solid Earth*, *126*(12), e2021JB022437. https://doi.org/10.1029/2021jb022437

Fei, H., Liu, Z., McCammon, C., & Katsura, T. (2020). Oxygen vacancy substitution linked to ferric iron in bridgmanite at 27 GPa. *Geophysical Research Letters*, *47*(6), e2019GL086296. https://doi.org/10.1029/2019gl086296

Frost, D. J., & Langenhorst, F. (2002). The effect of Al$_2$O$_3$ on Fe–Mg partitioning between magnesiowüstite and magnesium silicate perovskite. *Earth and Planetary Science Letters*, *199*(1–2), 227–241. https://doi.org/10.1016/s0012-821x(02)00558-7

Frost, D. J., Liebske, C., Langenhorst, F., McCammon, C. A., Trønnes, R. G., & Rubie, D. C. (2004). Experimental evidence for the existence of iron-rich metal in the Earth's lower mantle. *Nature*, *428*(6981), 409–412. https://doi.org/10.1038/nature02413

Fu, S., Yang, J., Karato, S. I., Vasiliev, A., Presniakov, M. Y., Gavriliuk, A. G., et al. (2019). Water concentration in single-crystal (Al, Fe)-bearing bridgmanite grown from the hydrous melt: Implications for dehydration melting at the topmost lower mantle. *Geophysical Research Letters*, *46*(17–18), 10346–10357. https://doi.org/10.1029/2019gl084630

Grüninger, H., Liu, Z., Siegel, R., Boffa Ballaran, T., Katsura, T., Senker, J., & Frost, D. J. (2019). Oxygen vacancy ordering in aluminous bridgmanite in the Earth's lower mantle. *Geophysical Research Letters*, *46*(15), 8731–8740. https://doi.org/10.1029/2019gl083613

Herring, C. (1950). Diffusional viscosity of a polycrystalline solid. *Journal of Applied Physics*, *21*(5), 437–445. https://doi.org/10.1063/1.1699681

Hirsch, L., & Shankland, T. (1991). Point defects in (Mg, Fe)SiO$_3$ perovskite. *Geophysical Research Letters*, *18*(7), 1305–1308. https://doi.org/10.1029/91gl01582

Holland, T., & Powell, R. (2011). An improved and extended internally consistent thermodynamic dataset for phases of petrological interest, involving a new equation of state for solids. *Journal of Metamorphic Geology*, *29*(3), 333–383. https://doi.org/10.1111/j.1525-1314.2010.00923.x

Horiuchi, H., Ito, E., & Weidner, D. J. (1987). Perovskite-type MgSiO$_3$; single-crystal X-ray diffraction study. *American Mineralogist*, *72*(3–4), 357–360.

Huang, R., Ballaran, T. B., McCammon, C. A., Miyajima, N., Dolejš, D., & Frost, D. J. (2021). The composition and redox state of bridgmanite in the lower mantle as a function of oxygen fugacity. *Geochimica et Cosmochimica Acta*, *303*, 110–136.

Irifune, T., Koizumi, T., & Ando, J.-I. (1996). An experimental study of the garnet-perovskite transformation in the system MgSiO$_3$–Mg$_3$Al$_2$Si$_3$O$_{12}$. *Physics of the Earth and Planetary Interiors*, *96*(2–3), 147–157. https://doi.org/10.1016/0031-9201(96)03147-0

Irifune, T., & Ringwood, A. (1993). Phase transformations in subducted oceanic crust and buoyancy relationships at depths of 600–800 km in the mantle. *Earth and Planetary Science Letters*, *117*(1–2), 101–110. https://doi.org/10.1016/0012-821x(93)90120-x

Ishii, T., Liu, Z., & Katsura, T. (2019). A breakthrough in pressure generation by a Kawai-type multi-anvil apparatus with tungsten carbide anvils. *Engineering*, *5*(3), 434–440. https://doi.org/10.1016/j.eng.2019.01.013

Ishii, T., Miyajima, N., Criniti, G., Hu, Q., Glazyrin, K., & Katsura, T. (2022). High pressure-temperature phase relations of basaltic crust up to mid-mantle conditions. *Earth and Planetary Science Letters*, *584*, 117472. https://doi.org/10.1016/j.epsl.2022.117472

Ishii, T., Shi, L., Huang, R., Tsujino, N., Druzhbin, D., Myhill, R., et al. (2016). Generation of pressures over 40 GPa using Kawai-type multi-anvil press with tungsten carbide anvils. *Review of Scientific Instruments*, *87*(2), 024501. https://doi.org/10.1063/1.4941716

Ito, E., Kubo, A., Katsura, T., Akaogi, M., & Fujita, T. (1998). High-pressure transformation of pyrope (Mg$_3$Al$_2$Si$_3$O$_{12}$) in a sintered diamond cubic anvil assembly. *Geophysical Research Letters*, *25*(6), 821–824. https://doi.org/10.1029/98gl00519

Ito, E., & Matsui, Y. (1978). Synthesis and crystal-chemical characterization of MgSiO$_3$ perovskite. *Earth and Planetary Science Letters*, *38*(2), 443–450. https://doi.org/10.1016/0012-821x(78)90119-x

Jackson, J. M., Zhang, J., & Bass, J. D. (2004). Sound velocities and elasticity of aluminous MgSiO$_3$ perovskite: Implications for aluminum heterogeneity in Earth's lower mantle. *Geophysical Research Letters*, *31*(10), L10614. https://doi.org/10.1029/2004gl019918

Janák, M., Ravna, E., & Kullerud, K. (2012). Constraining peak P–T conditions in UHP eclogites: Calculated phase equilibria in kyanite-and phengite-bearing eclogite of the Tromsø Nappe, Norway. *Journal of Metamorphic Geology*, *30*(4), 377–396. https://doi.org/10.1111/j.1525-1314.2011.00971.x

Jones, T. D., Maguire, R. R., van Keken, P. E., Ritsema, J., & Koelemeijer, P. (2020). Subducted oceanic crust as the origin of seismically slow lower-mantle structures. *Progress in Earth and Planetary Science*, *7*(1), 1–16. https://doi.org/10.1186/s40645-020-00327-1

Koizumi, S., Hiraga, T., Tachibana, C., Tasaka, M., Miyazaki, T., Kobayashi, T., et al. (2010). Synthesis of highly dense and fine-grained aggregates of mantle composites by vacuum sintering of nano-sized mineral powders. *Physics and Chemistry of Minerals*, *37*(8), 505–518. https://doi.org/10.1007/s00269-009-0350-y

Kojitani, H., Hisatomi, R., & Akaogi, M. (2007). High-pressure phase relations and crystal chemistry of calcium ferrite-type solid solutions in the system $MgAl_2O_4$-Mg_2SiO_4. *American Mineralogist*, *92*(7), 1112–1118. https://doi.org/10.2138/am.2007.2255

Kojitani, H., Katsura, T., & Akaogi, M. (2007). Aluminum substitution mechanisms in perovskite-type $MgSiO_3$: An investigation by Rietveld analysis. *Physics and Chemistry of Minerals*, *34*(4), 257–267. https://doi.org/10.1007/s00269-007-0144-z

Kubo, A., & Akaogi, M. (2000). Post-garnet transitions in the system $Mg_4Si_4O_{12}$–$Mg_3Al_2Si_3O_{12}$ up to 28 GPa: Phase relations of garnet, ilmenite and perovskite. *Physics of the Earth and Planetary Interiors*, *121*(1–2), 85–102. https://doi.org/10.1016/s0031-9201(00)00162-x

Larson, A. C., & Von Dreele, R. B. (1994). Gsas. Report lAUR. (pp. 86–748).

Liu, Z., Akaogi, M., & Katsura, T. (2019). Increase of the oxygen vacancy component in bridgmanite with temperature. *Earth and Planetary Science Letters*, *505*, 141–151. https://doi.org/10.1016/j.epsl.2018.10.014

Liu, Z., Ballaran, T. B., Huang, R., Frost, D. J., & Katsura, T. (2019). Strong correlation of oxygen vacancies in bridgmanite with Mg/Si ratio. *Earth and Planetary Science Letters*, *523*, 115697. https://doi.org/10.1016/j.epsl.2019.06.037

Liu, Z., Ishii, T., & Katsura, T. (2017a). Rapid decrease of $MgAlO_{2.5}$ component in bridgmanite with pressure. *Geochemical Perspectives Letters*, *5*, 12–18. https://doi.org/10.7185/geochemlet.1739

Liu, Z., McCammon, C., Wang, B., Dubrovinsky, L., Ishii, T., Bondar, D., et al. (2020). Stability and solubility of the $FeAlO_3$ component in bridgmanite at uppermost lower mantle conditions. *Journal of Geophysical Research: Solid Earth*, *125*(2), e2019JB018447. https://doi.org/10.1029/2019jb018447

Liu, Z., Nishi, M., Ishii, T., Fei, H., Miyajima, N., Ballaran, T. B., et al. (2017). Phase relations in the system $MgSiO_3$-Al_2O_3 up to 2300 K at lower mantle pressures. *Journal of Geophysical Research: Solid Earth*, *122*(10), 7775–7788. https://doi.org/10.1002/2017JB014579

McCammon, C. (1997). Perovskite as a possible sink for ferric iron in the lower mantle. *Nature*, *387*(6634), 694–696. https://doi.org/10.1038/42685

Murakami, M., Hirose, K., Yurimoto, H., Nakashima, S., & Takafuji, N. (2002). Water in Earth's lower mantle. *Science*, *295*(5561), 1885–1887. https://doi.org/10.1126/science.1065998

Navrotsky, A. (1999). A lesson from ceramics. *Science*, *284*(5421), 1788–1789. https://doi.org/10.1126/science.284.5421.1788

Navrotsky, A., Schoenitz, M., Kojitani, H., Xu, H., Zhang, J., Weidner, D. J., & Jeanloz, R. (2003). Aluminum in magnesium silicate perovskite: Formation, structure, and energetics of magnesium-rich defect solid solutions. *Journal of Geophysical Research*, *108*(B7), 2330. https://doi.org/10.1029/2002JB002055

Panero, W. R., Akber-Knutson, S., & Stixrude, L. (2006). Al_2O_3 incorporation in $MgSiO_3$ perovskite and ilmenite. *Earth and Planetary Science Letters*, *252*(1–2), 152–161. https://doi.org/10.1016/j.epsl.2006.09.036

Powell, R. (1978). *Equilibrium thermodynamics in petrology: An introduction*. Harper & Row.

Powell, R., & Holland, T. (1993). On the formulation of simple mixing models for complex phases. *American Mineralogist*, *78*(11–12), 1174–1180.

Shcheka, S. S., & Keppler, H. (2012). The origin of the terrestrial noble-gas signature. *Nature*, *490*(7421), 531–534. https://doi.org/10.1038/nature11506

Sun, S.-S. (1982). Chemical composition and origin of the Earth's primitive mantle. *Geochimica et Cosmochimica Act*a, *46*(2), 179–192. https://doi.org/10.1016/0016-7037(82)90245-9

Sun, S.-S., Nesbitt, R. W., & Sharaskin, A. Y. (1979). Geochemical characteristics of mid-ocean ridge basalts. *Earth and Planetary Science Letters*, *44*(1), 119–138. https://doi.org/10.1016/0012-821x(79)90013-x

Toby, B. H. (2001). EXPGUI, a graphical user interface for GSAS. *Journal of Applied Crystallograph*y, *34*(2), 210–213. https://doi.org/10.1107/s0021889801002242

Vanpeteghem, C. B., Angel, R., Ross, N., Jacobsen, S., Dobson, D., Litasov, K., & Ohtani, E. (2006). Al, Fe substitution in the $MgSiO_3$ perovskite structure: A single-crystal X-ray diffraction study. *Physics of the Earth and Planetary Interiors*, *155*(1–2), 96–103. https://doi.org/10.1016/j.pepi.2005.10.003

Walter, M. J., Kubo, A., Yoshino, T., Brodholt, J., Koga, K., & Ohishi, Y. (2004). Phase relations and equation-of-state of aluminous Mg-silicate perovskite and implications for Earth's lower mantle. *Earth and Planetary Science Letters*, *222*(2), 501–516. https://doi.org/10.1016/j.epsl.2004.03.014

Walter, M. J., Trønnes, R. G., Armstrong, L. S., Lord, O. T., Caldwell, W. A., & Clark, S. M. (2006). Subsolidus phase relations and perovskite compressibility in the system MgO–$AlO_{1.5}$–SiO_2 with implications for Earth's lower mantle. *Earth and Planetary Science Letters*, *248*(1–2), 77–89. https://doi.org/10.1016/j.epsl.2006.05.017

Weng, K., Mao, H. K., & Bell, P. M. (1981). *Lattice parameters of the perovskite phase in the system $MgSiO_3$-$CaSiO_3$-Al_2O_3* (Vol. 81, pp. 273–277). Carnegie Institute Washington: Year Book.

Xu, Y., McCammon, C., & Poe, B. T. (1998). The effect of alumina on the electrical conductivity of silicate perovskite. *Science*, *282*(5390), 922–924. https://doi.org/10.1126/science.282.5390.922

Yagi, T., Okabe, K., Nishiyama, N., Kubo, A., & Kikegawa, T. (2004). Complicated effects of aluminum on the compressibility of silicate perovskite. *Physics of the Earth and Planetary Interiors*, *143*, 81–91. https://doi.org/10.1016/j.pepi.2003.07.020

Yamada, H., Matsui, Y., & Ito, E. (1983). Crystal-chemical characterization of $NaAlSiO_4$ with the $CaFe_2O_4$ structure. *Mineralogical Magazine*, *47*(343), 177–181. https://doi.org/10.1180/minmag.1983.047.343.07

Yamamoto, T., Yuen, D. A., & Ebisuzaki, T. (2003). Substitution mechanism of Al ions in $MgSiO_3$ perovskite under high pressure conditions from first-principles calculations. *Earth and Planetary Science Letters*, *206*(3–4), 617–625. https://doi.org/10.1016/s0012-821x(02)01099-3

Zhang, J., & Weidner, D. J. (1999). Thermal equation of state of aluminum-enriched silicate perovskite. *Science*, *284*(5415), 782–784. https://doi.org/10.1126/science.284.5415.782